AIP Advances

Perovskite solar cells with a hybrid electrode structure

Cite as: AIP Advances **9**, 125037 (2019); https://doi.org/10.1063/1.5127275
Submitted: 12 September 2019 . Accepted: 03 December 2019 . Published Online: 23 December 2019

Yinghong Hu, Gede W. P. Adhyaksa, Giovanni DeLuca, Alexandr N. Simonov, Noel W. Duffy, Elsa Reichmanis, Udo Bach, Pablo Docampo, Thomas Bein, Erik C. Garnett, Anthony S. R. Chesman, and Askhat N. Jumabekov

Perovskite solar cells with a hybrid electrode structure

Cite as: AIP Advances 9, 125037 (2019); doi: 10.1063/1.5127275
Submitted: 12 September 2019 • Accepted: 3 December 2019 •
Published Online: 23 December 2019

Yinghong Hu,[1,2,a] Gede W. P. Adhyaksa,[3,a] Giovanni DeLuca,[1,4,5,6] Alexandr N. Simonov,[7] Noel W. Duffy,[8] Elsa Reichmanis,[5,6] Udo Bach,[4,9] Pablo Docampo,[2,10] Thomas Bein,[2] Erik C. Garnett,[3] Anthony S. R. Chesman,[1,9,b] and Askhat N. Jumabekov[1,11,b]

AFFILIATIONS

[1] CSIRO Manufacturing, Clayton, Victoria 3168, Australia
[2] Department of Chemistry and Center for NanoScience (CeNS), LMU Munich, 81377 Munich, Germany
[3] Center for Nanophotonics, AMOLF, 1098 XG Amsterdam, The Netherlands
[4] Department of Chemical Engineering, Monash University, Clayton, Victoria 3800, Australia
[5] School of Chemistry and Biochemistry, Georgia Institute of Technology, Atlanta, Georgia 30332, USA
[6] School of Chemical and Biomolecular Engineering, Georgia Institute of Technology, Atlanta, Georgia 30332, USA
[7] School of Chemistry and The ARC Centre of Excellence for Electromaterials Science, Monash University, Clayton, Victoria 3800, Australia
[8] CSIRO Energy, Clayton, Victoria 3168, Australia
[9] Melbourne Centre for Nanofabrication, Clayton, Victoria 3168, Australia
[10] School of Electrical and Electronic Engineering, Newcastle University, Merz Court, NE1 7RU Newcastle upon Tyne, Newcastle, United Kingdom
[11] Department of Physics, Nazarbayev University, Nur-Sultan 010000, Kazakhstan

[a] **Contributions:** Y. Hu and G. W. P. Adhyaksa contributed equally to this work.
[b] **Authors to whom correspondence should be addressed:** anthony.chesman@csiro.au and askhat.jumabekov@nu.edu.kz

ABSTRACT

Perovskite solar cells (PSCs) with a novel hybrid electrode structure, in which a single device can operate with either a vertical (sandwich) or lateral (back-contact) configuration of contacts, are demonstrated in this work. The hybrid structure was achieved by depositing an additional anode on top of a prefabricated back-contact PSC device, giving a final device with three electrodes—one shared cathode and two anodes. Device performances are tested and evaluated for both operation modes, and a semianalytical model along with coupled optoelectronic simulations is used to rationalize the experimental results. It is determined that due to the intrinsically narrow depletion region near the contact interfaces, the charge collection efficiency in the back-contact device structure appears to be significantly lower compared to the sandwich device structure. This finding provides an insight into the cause of the performance disparity between these two architectures.

Organic-inorganic hybrid perovskites are one of the most promising low cost and solution-processable photovoltaic (PV) materials.[1,2] To date, perovskite solar cells (PSCs) with a simple *n-i-p* sandwich structure [Fig. 1(a)] have yielded power conversion efficiencies (PCEs) above 25%, surpassing the PCEs of polycrystalline Si devices (~22%).[3] Similar to their Si-based analogs, it is predicted that perovskites can achieve even higher PCEs using a back-contact device architecture.[4,5] The first operational back-contact perovskite solar cell (BC-PSC) incorporated a quasi-interdigitated electrode (QIDE) in which a microarray of anodes is placed above the planar cathode [Fig. 1(b)].[6–8] This robust architecture is more suitable for perovskite photoabsorbers, as BC-PSCs using a

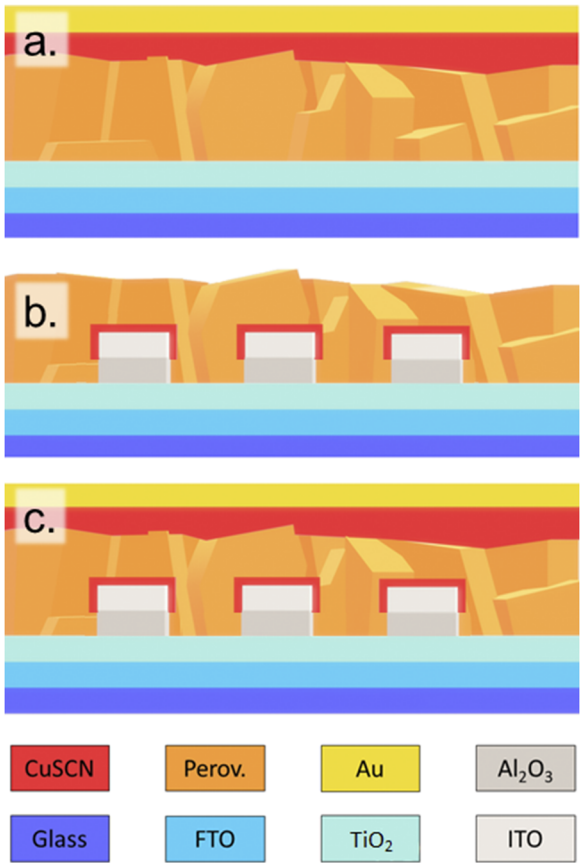

FIG. 1. (a) Sandwich PSC, (b) back-contact PSC based on QIDEs, and (c) hybrid-structured PSC.

conventional interdigitated back contact require a reduction in electrode spacing to accommodate the shorter carrier diffusion lengths compared to silicon, likely leading to a prohibitive increase in electrode defects.[9,10] Despite this advantage, the reported performances of BC-PSCs incorporating QIDEs have plateaued at 5%, suggesting that a greater understanding of the device physics is required.[7]

In principle, the PCEs of BC-PSCs and conventional sandwich PSCs should be comparable,[4,9,10] but the difference in record efficiencies between the two architectures indicates that there may be inherent issues with the former structure. However, even if sandwich and back-contact PSCs are fabricated using the same materials, comparing the underlying physics of the architectures remains complicated, as the two structures will use active layers with different properties, i.e., BC-PSCs will give rougher perovskite layers due to the electrode structure or the sandwich PSC will suffer transmission losses due to the substrate and its active layers. Overcoming these issues requires the creation of a hybrid-structured device in which the back-contact and sandwich modes (SWMs) are incorporated into a single solar cell sharing an identical active area. This would allow for the direct comparison of the PSC performance in either the back-contact or sandwich mode using exactly the same perovskite photoabsorber layer.

Recently, DeLuca *et al.* reported bifacial BC-PSCs incorporating transparent back-contacts with illumination from either side giving similar performance [Fig. 1(b)].[11] For our purposes, such a device is an excellent candidate to realize the aforementioned PSC with a hybrid structure with the deposition of an additional electrode system on top of the perovskite layer of a BC-PSC, yielding a device with one common cathode and two anodes (or vice versa) [Fig. 1(c)]. Herein, we demonstrate an example of a PSC with such a hybrid electrode structure using transparent QIDEs and perform a comparative analysis between the sandwich and back-contact operation modes.

The first stage of building a hybrid-structured PSC was to fabricate BC-PSCs using transparent QIDEs, as described by DeLuca *et al.*[11] A cross-sectional scanning electron microscope (SEM) image of a hybrid device shows that the ~350 nm $Cs_{0.05}FA_{0.79}MA_{0.16}PbI_{2.49}Br_{0.51}$ perovskite layer uniformly covers the transparent QIDE, which consists of a microstructured anode [~1.5 μm wide indium tin oxide "fingers" with a CuSCN coating (ITO|CuSCN) spaced every ~2.5 μm] on a continuous cathode [fluorine-doped tin oxide with a TiO_2 layer (FTO|TiO_2) on glass] (Fig. 2). The anode and cathode are separated by an ~100 nm Al_2O_3 insulating layer to prevent shorting. The device was completed by spin coating an ~60 nm CuSCN hole transporting layer (HTL) to conformally cover the exposed perovskite surface, followed by evaporating ~80 nm of gold through a mask to form the top electrode for the sandwich part (see Fig. S1 of the supplementary material). A more detailed description of the fabrication process is given in the supplementary material. A photograph of the device is shown in Fig. S2 of the supplementary material.

The J–V characteristics of the hybrid-structured PSC devices were recorded for both operation modes with rear (glass) side illumination. The sandwich mode (SWM) operates when the back-contact mode (BCM) is open circuited ($J_{BCM} = 0$), and vice versa, allowing the SWM and BCM to operate independently of each other. Figure 3 shows J–V curves under 1 sun AM1.5G illumination and in the dark. The relevant photovoltaic parameters [short-circuit current density (J_{SC}), open-circuit voltage (V_{OC}), fill factor (FF), and PCE] for both

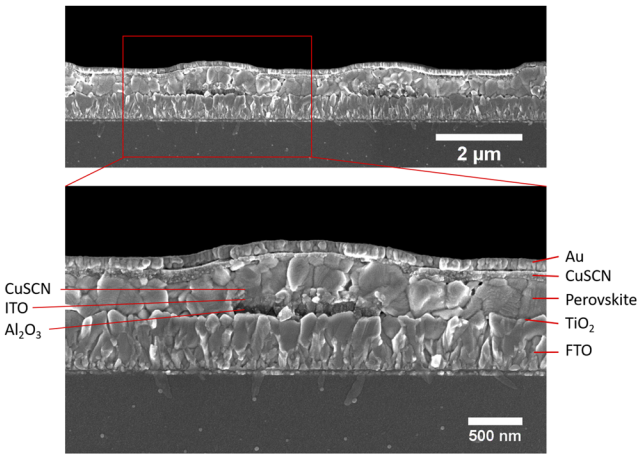

FIG. 2. SEM cross-sectional micrograph of a hybrid-structured PSC device.

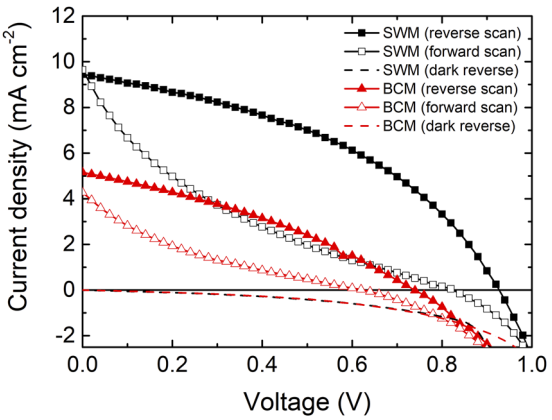

FIG. 3. *J–V* characteristics (scan rate 0.2 V s^{-1}) of a hybrid-structured PSC device operated in sandwich (*black*) and back-contact (*red*) modes under 1 sun illumination (solid lines with symbols) and in the dark (dashed lines). Empty and filled symbols show forward (open-circuit to short-circuit direction) and reverse (short-circuit to open-circuit) scans, respectively; solid lines are guides to eyes.

operation modes are listed in Table I. The disparity between forward and reverse scans is due to the hysteresis phenomenon, which is commonly ascribed to the existence of mobile ions within the perovskite material.[1,6–9,11] Both operation modes show similar levels of hysteresis (taking the ratio of reverse to forward scan). The stabilized power output for PSC devices operated in sandwich (*black*) and back-contact (*red*) modes under 1 sun illumination was obtained from maximum power point tracking experiments (see Fig. S3). The statistical data for photovoltaic parameters for both operation modes are listed in Table S1 of the supplementary material.

The device has an identical active area (0.08 cm^2) for both SWM and BCM configurations that, therefore, differ only in the geometry of their electrical contacts (Figs. 2 and S2). This suggests that the SWM and BCM configurations should have the same attainable optical power at zero voltage (J_{sc}). However, the experiment shows that the J_{sc} of the SWM and BCM are different and far below the theoretical maximum potential J_{sc} calculated based on wave-optic simulations (accounting for all interference, parasitic absorption, transmission, and reflection losses).[11] This indicates that there may be a collection loss associated with the device electronic configuration, which has not been considered earlier.[4,10,11]

To understand this discrepancy, the *J-V* curve characteristics were first modeled using a simple triple-diode equation to capture the characteristics of the *p-i-n* layers without prior knowledge of the device contact geometry. The goal of the model is to provide an initial estimate of the effective collection length (L_c) by evaluating the *J-V* curve characteristics between the SWM and BCM configurations,

$$J(V) = J_{0p}\left[e^{\left(\frac{V}{n_{0p}(kT/q)}\right)} - 1\right] + J_{0i}\left[e^{\left(\frac{V+J(V)R_S}{n_{0i}(kT/q)}\right)} - 1\right] + J_{0n}\left[e^{\left(\frac{V}{n_{0n}(kT/q)}\right)} - 1\right] - \frac{V}{R_{SH}} - J_{sc}. \quad (1)$$

This model assumes that the collection efficiency is 100% and is independent of the applied voltage; however, this assumption is subsequently corrected (see the discussion below). The n_{0p}, n_{0i}, and n_{0n} are the diode-ideality factors (see Table S2 of the supplementary material) at the *p*-, *i*-, and *n*-type layers, respectively (obtained numerically using global optimization to minimize errors between experimental and fitting). The (kT/q) is the thermal voltage at 300 K, R_S is the series resistance, R_{SH} is the shunt resistance, and J_{sc} is the theoretical maximum short-circuit current density (obtained from the optical simulation). The J_{0p}, J_{0i}, and J_{0n} are dark saturation current densities at the *p*-, *i*-, and *n*-type active layers, respectively. J_{0p} and J_{0n} contain information on the depletion regions from which the initial guess of L_c can be interpolated (details in the supplementary material). This model alone is insufficient to fit the whole experimental data (even if global iterations of R_S and R_{SH} are taken into account) but is sufficient to obtain an initial estimation of the L_c for each configuration.

Next, a model developed within a reciprocal relation between carrier injection and collection was used to determine in greater detail the source of the discrepancy and to explain the difference in collection efficiencies between sandwich and back-contact geometries.[12–15] The collection efficiency is therefore not only limited by the device geometry but also by the voltage applied to the respective structures. The collection efficiency (η_c) is formulated as (details in the supplementary material)[12–15]

$$\eta_c(V) = 1 - \left(\frac{\eta_i(V)\eta_{out}(V)}{A(\lambda)\phi_{sun}(\lambda)\phi_{bb}(\lambda)}\right)\frac{PLQY(V)}{J_D(V)}, \quad (2)$$

where η_i is the injection efficiency, η_{out} is the light out-coupling efficiency, $A(\lambda)$ is the absorption of the active layer, $\phi_{sun}(\lambda)$ is the 1 sun irradiation, and $\phi_{bb}(\lambda)$ is the black-body radiation, all of which are the same for both configurations. In contrast, the voltage-dependent photoluminescence quantum yield $[PLQY(V)]$ and voltage dependent dark-current $[J_D(V)]$ containing the triple diode equation vary and are therefore dependent on the two contact geometries. This highlights the importance of Eq. (1) in obtaining the initial estimate of L_c to be used in Eq. (2), from which after subsequent iterations, we can extract the effective collection length (L_c). Figure 4(a) depicts the collection efficiency as a function of applied voltage [Eq. (2)] and shows that the collection efficiency is indeed not constant across an applied voltage (i.e., the quasi-Fermi level splitting is not constant) and is dependent on the collection length (L_c) as interpolated from the model. Based on this model, L_c is at least an order of magnitude shorter in the BCM geometry than in the standard SWM configuration. Open circuit photovoltage decay (OCVD) measurements reveal a shorter electron lifetime for the BCM than for the SWM by a factor of ~4 (Fig. S4), which supports the findings of this model.

TABLE I. Photovoltaic parameters for the SWM and BCM under 1 sun illumination.

Operation modes	V_{oc} (V)	J_{sc} (mA cm^{-2})	FF (%)	PCE (%)
SWM (reverse scan)	0.92	9.45	42.2	3.7
SWM (forward scan)	0.82	9.65	14.3	1.1
BCM (reverse scan)	0.74	5.16	33.2	1.3
BCM (forward scan)	0.62	4.28	15.0	0.4

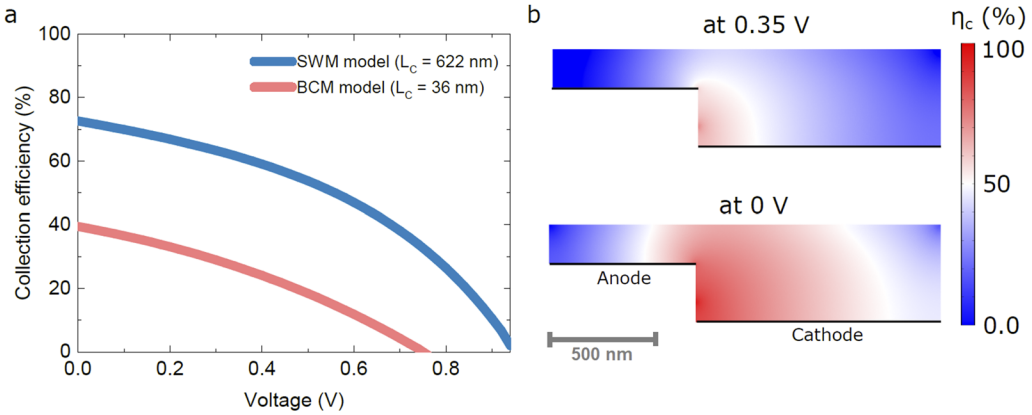

FIG. 4. Modeling the voltage-dependent collection efficiency. (a) Collection efficiency using a semianalytical model showing the contrast between BCM and SWM configurations. (b) Spatial dependence collection efficiency for the BCM configuration.

To provide a more intuitive picture, a fully coupled optical-electrical simulation was performed to map the spatial dependence of collection efficiency on the BCM geometry [Fig. 4(b)]. This map is constructed by "pumping" a uniform generation rate on top of the spatially dependent generation rate in every spatial point of the map and "probing" a change in total collected majority carriers. The maximum collection efficiency takes place near the adjacent contacts where an intense space-charge region is expected. This is consistent with experimental findings reported previously.[6] As applied bias, the collection efficiency is reduced where the range of its distance is much shorter than the half-pitch size demonstrated here (36 nm collection length vs 1.25 μm pitch). In other words, the electric field required for charge separation is reduced with the distance from the closest adjacent two contacts. Note that in the experimental data, the collection efficiency is effectively zero at voltages close to V_{oc}, meaning that there is no charge extraction at V_{oc}, and is equivalent to the maximum injection efficiency in the dark condition (maximum quasi-Fermi level splitting).

BC-PSCs must overcome the limitations of their collection efficiencies to achieve their maximum potential efficiencies. To solve this problem, a large depletion region can be created to improve the charge collection efficiency, for example, not only near the contacts but also at the grain boundaries.[16] Recently, Tainter *et al.* showed that effective charge segregation (probably at the grain boundaries) may improve long-range charge extraction in a similar device geometry.[17] Grain boundaries may form an array of *p-i-n* junctions through the interfaces between the two electrodes and that is conceptually equivalent to the effective depletion region discussed here. However, in our case, it seems that only the interfaces between active layers and contacts serve as *p-i-n* junctions. Engineering the back-contact geometry by utilizing a cross-grating back-contact may break this limitation by localizing larger carrier generation around the contact geometry.[5] In addition to this, the importance of the voltage dependent collection efficiency should be considered in interpreting any data obtained from *operando* characterizations of thin-film semiconductors when using a back-contact geometry as a platform.

For the purpose of simplifying the analysis and modeling of the devices presented here, we considered the influence of the back-contact electrode on the operation of the devices in SWM configuration to be negligible. However, comparing the performances for our device in SWM configuration with standard sandwich-type planar PSC devices reported in the literature requires caution, as the influence of the embedded back-contact electrodes on device performance in SWM configuration is yet to be explored, and the low efficiencies obtained suggest that the presence of the back-contact electrodes may have a detrimental effect. Nevertheless, the objective of utilizing this hybrid electrode structure is to reveal the inherent issues with the back-contact architecture, in particular, and to understand the mechanisms through which the electrodes are limiting device performance. Both the experimental and theoretical results in this study suggest that the issue with charge collection needs to be addressed for the back-contact architecture to fulfill its potential.

In summary, the fabrication of a PSC device with a hybrid structure was achieved by depositing a top electrode onto a back-contact device with t-QIDEs. The performance of the device in both operation modes was tested, with the PCE of the SWM being three times higher than that of the BCM. The discrepancy between the PCEs of the SWM and BCM operation modes was rationalized using a coupled optical-electrical simulation method and a semianalytical model. The BCM suffers from a charge collection efficiency at least an order of magnitude lower than the SWM configuration because of its intrinsically narrow depletion region across the contact interfaces. Future work on the back-contact perovskite solar cell should focus on understanding and overcoming this fundamental limitation, such as through interfacial doping.

See the supplementary material for experimental details including materials, fabrication of transparent quasi-interdigitated electrodes, deposition of the CuSCN layer, PV device fabrication, characterization details, and details of the solar simulation setup and device structures, J–V curves, photovoltaic parameters, open circuit photovoltage decay curves, electron lifetime estimations, and physical parameters used in simulations of collection efficiency.

ACKNOWLEDGMENTS

Y.H. acknowledges funding from the DFG Excellence Cluster "Nanosystems Initiative Munich" (NIM), the Center for NanoScience (CeNS), and the Bavarian Collaborative Research Program "Solar Technologies Go Hybrid" (SolTech). A.N.S. and U.B. are grateful to the Australian Research Council for financial support (Grant Nos. CE140100012 and CE170100026, respectively). G.D. is grateful for support from the NSF EAPSI program (Grant No. OISE 1713327). E.R. appreciates financial support from the National Science Foundation (Grant No. NSF ECCS 1665279). A.N.J. acknowledges an Office of the Chief Executive Postdoctoral Fellowship (CSIRO Manufacturing) and financial support from FDCRG (Grant No. 110119FD4512) and SPG fund (Nazarbayev University). This work was performed in part at the Melbourne Centre for Nanofabrication (MCN) in the Victorian Node of the Australian National Fabrication Facility (ANFF). The authors would like to thank Mr. Mark Greaves from CSIRO Manufacturing for his help with SEM imaging. E.C.G. and G.W.P.A. acknowledge financial support from the European Research Council (Grant No. 337328), "NanoEnabledPV." The authors also acknowledge the financial support from the Australian Renewable Energy Agency (ARENA) and the Australian Centre for Advanced Photovoltaics (ACAP).

REFERENCES

[1] A. Rajagopal, K. Yao, and K.-Y. A. Jen, "Toward perovskite solar cell commercialization: A perspective and Research roadmap based on interfacial engineering," Adv. Mater. **30**, 1800455 (2018).

[2] A. Kojima, K. Teshima, Y. Shirai, and T. Miyasaka, "Organometal halide perovskites as visible-light sensitizers for photovoltaic," J. Am. Chem. Soc. **131**, 6050–6051 (2009).

[3] https://www.nrel.gov/pv/cell-efficiency.html.

[4] T. Ma, Q. Song, D. Tadaki, M. Niwano, and A. Hirano-Iwata, "Unveil the full potential of integrated-back-contact perovskite solar cells using numerical simulation," ACS Appl. Energy Mater. **1**, 970–975 (2018).

[5] G. W. P. Adhyaksa, E. Johlin, and E. C. Garnett, "Nanoscale back contact perovskite solar cell design for improved tandem efficiency," Nano Lett. **17**, 5206–5212 (2017).

[6] A. N. Jumabekov, E. Della Gaspera, Z.-Q. Xu, A. S. R. Chesman, J. van Embden, S. A. Bonke, Q. Bao, D. Vak, and U. Bach, "Backcontacted hybrid organic–inorganic perovskite solar cells," J. Mater. Chem. C **4**, 3125–3130 (2016).

[7] Q. Hou, D. Bacal, A. N. Jumabekov, W. Li, Z. Wang, X. Lin, S. H. Ng, B. Tan, Q. Bao, A. S. R. Chesman, Y. B. Cheng, and U. Bach, "Back-contact perovskite solar cells with honeycomb-like charge collecting electrodes," Nano Energy **50**, 710–716 (2018).

[8] A. N. Jumabekov, J. A. Lloyd, D. M. Bacal, U. Bach, and A. S. R. Chesman, "Fabrication of back-contact electrodes using modified natural lithography," ACS Appl. Energy Mater. **1**, 1077–1082 (2018).

[9] L. M. Pazos-Outón, M. Szumilo, R. Lamboll, J. M. Richter, M. Crespo-Quesada, M. Abdi-Jalebi, H. J. Beeson, M. Vrućinić, M. Alsari, H. J. Snaith, D. Ehrler, R. H. Friend, and F. Deschler, "Photon recycling in lead iodide perovskite solar cells," Science **351**, 1430–1433 (2016).

[10] X. Lin, A. N. Jumabekov, N. N. Lal, A. R. Pascoe, D. E. Gómez, N. W. Duffy, A. S. R. Chesman, K. Sears, M. Fournier, Y. Zhang, Q. Bao, Y. B. Cheng, L. Spiccia, and U. Bach, "Dipole-field-assisted charge extraction in metal-perovskite-metal back-contact solar cells," Nat. Commun. **8**, 613 (2017).

[11] G. DeLuca, A. N. Jumabekov, Y. Hu, A. N. Simonov, J. Lu, B. Tan, G. W. P. Adhyaksa, E. C. Garnett, E. Reichmanis, A. S. R. Chesman, and U. Bach, "Transparent quasi-interdigitated electrodes for semitransparent perovskite back-contact solar cells," ACS Appl. Energy Mater. **1**, 4473–4478 (2018).

[12] C. Donolato, "A reciprocity theorem for charge collection," Appl. Phys. Lett. **46**, 270–272 (1985).

[13] K. Toprasertpong, A. Delamarre, Y. Nakano, J.-F. Guillemoles, and M. Sugiyama, "Generalized reciprocity relations in solar cells with voltage-dependent carrier collection: Application to p-i-n junction devices," Phys. Rev. Appl. **11**, 024029 (2019).

[14] G. W. P. Adhyaksa, S. Brittman, H. Āboliņš, A. Lof, X. Li, J. D. Keelor, Y. Luo, T. Duevski, R. M. A. Heeren, S. R. Ellis, D. P. Fenning, and E. C. Garnett, "Understanding detrimental and beneficial grain boundary effects in halide perovskites," Adv. Mat. **30**, 1804792 (2018).

[15] P. Cui, D. Wei, J. Ji, H. Huang, E. Jia, S. Dou, T. Wang, W. Wang, and M. Li, "Planar p-n homojunction perovskite solar cells with efficiency exceeding 21.3%," Nat. Energy **4**, 150–159 (2019).

[16] C.-C. Zhang, Z.-K. Wang, S. Yuan, R. Wang, M. Li, F. M. Jimoh, L.-S. Liao, and Y. Yang, "Polarized ferroelectric polymers for high-performance perovskite solar cells," Adv. Mater. **31**, 1902222 (2019).

[17] G. D. Tainter, M. T. Hörantner, L. M. Pazos-Outón, R. D. Lamboll, H. Āboliņš, T. Leijtens, S. Mahesh, R. H. Friend, H. J. Snaith, H. Joyce, and F. Deschler, "Long-range charge extraction in back-contact perovskite architectures via suppressed recombination," Joule **3**, 1301–1313 (2019).